This is the preprint of the contribution published as:

The publisher's version is available at:

A fibre-optical method for monitoring barite precipitation at high pressure/high temperature conditions

Jörg Zotzmann[a,*], Nele Hastreiter[a,1], Sathish Mayanna[a,2], Thomas Reinsch[a,3], Simona Regenspurg[a]

[a]Helmholtz Centre Potsdam, German Research Centre for Geosciences, Telegrafenberg, 14473 Potsdam, Germany

ABSTRACT

Monitoring and controlling of mineral precipitation is a major challenge in several industry segments such as oil and gas or geothermal energy. Especially at elevated pressures, temperatures, and salinities, these reactions are poorly understood and difficult to predict. Real-time monitoring under such conditions, however, is crucial for reduction or prevention of scaling as well as for process modelling. In this study, a novel fibre-optical method for monitoring the barite precipitation process at high pressures and high temperatures was developed and tested. The applicability of a fibre-optical sensor was demonstrated and kinetic data derived from experiments using synthetic fluids that were oversaturated with barite. The ionic strength was varied between 0 and 5 mol/l NaCl to simulate geothermal brines typically found in deep sedimentary reservoirs. Experiments were performed at 25 and 150 °C. For the studied variations it was found that the ionic strength had a strong impact on the barite precipitation rate whereas temperature had only a minor influence. The kinetic rate constants were decreasing with increasing salinity ranging from 9 to 0.4 $l \cdot mol^{-1} \cdot s^{-1}$ at 25 °C and from 8.6 to 0.66 $l \cdot mol^{-1} \cdot s^{-1}$ at 150 °C.

1. INTRODUCTION

Mineral precipitation (scaling) is one of the limiting factors for an efficient operation of applications where water with dissolved scale-forming minerals is involved (MacAdam and Jarvis 2015). Barite is a well-known scale-forming mineral in oil and gas wells as well as in geothermal installations (Yuan and Todd 1991, Scheiber et al. 2014). The mineral causes severe problems ranging from clogging of pipes to the damage of installations and reducing reservoir permeability. Well productivity and in particular the injectivity of the processed fluids often substantially deteriorate over time due to precipitation in the surface and subsurface installations. Mineral precipitation in geothermal plants occurs due to supersaturation of minerals caused by changes in the chemical equilibria during processing (production, heat exchange and re-injection) of geothermal fluids. In particular fluids from highly saline, sedimentary geothermal reservoirs are prone to scaling but are poorly understood. Due to unknown solubilities and activity coefficients at extreme conditions scaling can hardly be predicted. Barite is one of the most frequently encountered scale minerals in such systems (Regenspurg et al. 2015, Canic et al. 2015, Scheiber et. al 2014).

The control of scaling such as barite in terms of reduction or prevention is of utmost importance for a sustainable operation of a geothermal plant. Scaling mitigation methods typically comprise the addition of chemicals to the brine which inhibit the minerals to precipitate. However, those inhibitors often are expensive and the efficiency strongly depends on the physical and chemical properties of the geothermal fluid. The understanding of type and kinetics of the respective precipitations and the testing/optimisation of the inhibitors in the particular fluid is necessary (Zotzmann et al. 2018). However, the observation of mineral precipitations and the measurements of influencing parameters in geothermal plants or fields is still hard to realise due to the harsh conditions typically found in geothermal systems such as high temperatures, high pressures, high ionic strength, complex chemical composition and high corrosiveness of the fluids. Thus, the demand for robust methods to monitor scaling processes at elevated pressure and temperature conditions and in a wide range of salinities is high. For prediction and control of scaling processes it is also important to understand the rate of the reaction, which is controlled by the kinetic properties of the respective precipitating mineral. Scaling is often kinetically hindered and thus occurs not always directly after supersaturation is reached. The

rates of precipitation reactions depend on various factors such as concentrations of the reaction partners, pressure, temperature, salinity and catalytic effects of surfaces or crystal seeds.

The objective of this study was to develop and test a fibre-optical method to observe and understand barite precipitation. Synthetic fluids resembling sedimentary basin brines were monitored under high pressure/high temperature conditions and the influence of ionic strength as well as temperature on the precipitation was investigated. The barite precipitation was monitored and kinetic rate constants were derived from the experimental fibre-optical data.

Over the past two decades, fibre optics have become of special interest in research to be used as real-time sensors for different kinds of measurements due to their advantages in comparison to conventional electric sensors (Udd and Spillman Jr. 2011, Wang and Wolfbeis 2016, Shukla et al. 2019, Bremer et al 2017). Fibre-optical sensors are typically cheap, light weight devices, robust, flexible for installation and applications, highly sensitive and applicable for multifunctional sensing (Fidanboylu and Efendioglu 2009). Fibre-optical sensors have already been considered as a possible method for real-time detection of processes such as the precipitation of silica, calcite or silver chloride (Philip-Chandy et al. 2000; Okazaki et al. 2015; Okazaki et al. 2017). The measurement was found to be sensitive to the scale layer height and average crystal contact area on the optical fibre core and thus providing a principle for monitoring surface crystal growth (Boerkamp et al. 2007; Boerkamp et al. 2013). The applicability of the fibre-optical sensors for *in-situ* measurement of nucleation and crystal growth was also shown by using optical fibres from organic polymers such as poly(methyl methacrylate). The obtained signals correlated with the growth of the scale crystals on the surface of the fibre (Wallace et al. 2008). However, the use of organic polymer fibres is limited to moderate temperatures. The resilience of fibre-optical sensors even at harsh conditions prevailing in geothermal fluids was shown by Okazaki et al. (2015, 2017). After laboratory testing, the sensors were applied in field tests at geothermal sites detecting calcite and silica scales respectively. The transmittance response was analysed over a wide range of wavelengths and showed that the sensor detection for near infrared light was sufficiently sensitive for the intended application. The capability of monitoring scale formation in a geothermal environment was confirmed and the evaluation of the effect of scale inhibitors investigated.

The principle of fibre-optical sensors applied for scaling detection is based on the attenuation of total internal reflection (TIR) that occurs along the boundary of a fibre core when it is used for guiding light. The light is totally reflected at the interface between the fibre core and its environment if the angle of incidence is greater than the critical angle θ_{cr}. θ_{cr} defines the minimum incident angle for totally reflected light under the precondition that the refractive index of the core (n_1) is higher than the refractive index of the environment (n_2). According to Snell's law: $\theta_{cr} = \arcsin(n_2/n_1)$ the range of incident angles for TIR decreases with an increasing quotient of the refractive indices n_2/n_1 (Harmon 2001). Hence, TIR is mainly defined by the difference in the refractive indices between the fibre core and the environment. For cladded fibre cores, the cladding exhibits a refractive index considerably lower than that of the core and ensures TIR for a wide range of incident angles. If the cladding is removed, the range of incident angles for TIR depends on the refractive index of the medium the fibre is immersed in. Increasing the refractive index of the medium leads to an increase of θ_{cr} so that the range of incident angles and thus the portion of light undergoing TIR will be decreased. That applies to a surrounding aqueous solution as well as to scale crystals forming on the surface of the fibre core. Therefore, scaling crystals with a higher refractive index than the fibre material cause refraction of the light at the contact area with the fibre surface and thereby reduce the light passing through by TIR (figure 1).

On the surface of optical fibres that conduct light by TIR an evanescent wave forms that propagates along the core surface (Anderson, Taitt 2008). It exhibits a very small penetration depth into the surrounding medium with power dropping exponentially with distance but does not lead to a loss of reflected light as long as it is not disturbed. The fibre is typically cladded with a layer of transparent polymer that ensures an undisturbed propagation of the evanescent wave. If the cladding of the fibre is removed, however, the evanescent wave can interact with the environment by absorption or scattering (figure 1) resulting in a loss of the reflected light and thus to an attenuated total reflection (ATR) inside the fibre core (Vardeny 2002, Chyad et al. 2013).
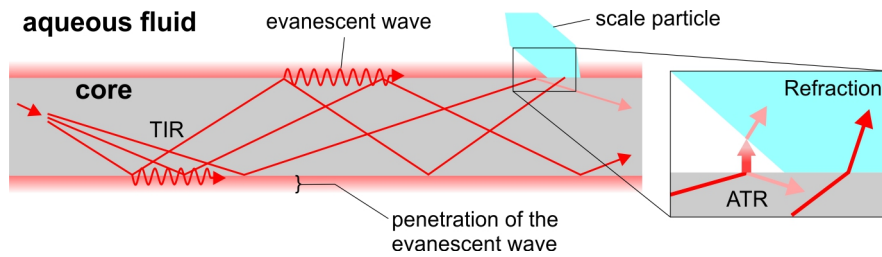
Fig. 1: Transmission of monochromatic light through the exposed core of an optical fibre with a scale particle having a refractive index higher than that of the fluid surrounding the core causing scattering of the evanescent wave.

Light attenuation (A) within an optical fibre is typically measured in dB with the transmitted light power (P) related to the power of the initial light from the source (P_0) according to equation (1) or in dBm if P is related to a theoretical P_0 of 1 mW as in equation (2). The transmitted light power (P in mW) can be derived from the attenuation as shown in equation (3).

(1) $\qquad A\,[\mathrm{dB}] = -10 \cdot \lg\left(\frac{P}{P_0}\right)$

(2) $\qquad A\,[\mathrm{dBm}] = -10 \cdot \lg\left(\frac{P}{1\,\mathrm{mW}}\right)$

(3) $\qquad P\,[\mathrm{mW}] = 10^{-\frac{A\,(\mathrm{dBm})}{10}}$

In saline geothermal brines from sedimentary reservoirs (e.g. from the Northern German Basin) the concentration of the sulfate ions is typically found in a 5 to 10 times excess compared to the barium ions (Regenspurg et al. 2010). The proportion of the starting concentration in the synthetic fluids of this study were therefore chosen as $[\mathrm{SO_4^{2-}}]_0 = 10[\mathrm{Ba^{2+}}]_0$. The barite precipitation follows the chemical reaction (4). The barite precipitation follows a second order kinetic rate law (Christy and Putnis 1993, Kühn et al. 1997, Banks et al. 2014). In order to obtain rate constants (k) the experimental data are typically plotted according to the integrated rate law of a 2$^{\text{nd}}$ order reaction and a linear fit is applied. Rate constants can then be derived from the slope of the linear fit. The kinetic rate law of the barite precipitation as well as the integration under different concentration conditions is shown in table 1.

(4) $\qquad \mathrm{Ba^{2+} + SO_4^{2-} \rightarrow BaSO_4}\downarrow$

Tab. 1: Kinetic rate law of a 2$^{\text{nd}}$ order barite precipitation reaction.

rate law:	$r = \dfrac{-d[\mathrm{Ba^{2+}}]}{dt} = k[\mathrm{Ba^{2+}}][\mathrm{SO_4^{2-}}]$		
concentration conditions:	$[\mathrm{Ba^{2+}}]_0 = [\mathrm{SO_4^{2-}}]_0$	$[\mathrm{Ba^{2+}}]_0 \neq [\mathrm{SO_4^{2-}}]_0$	$[\mathrm{SO_4^{2-}}]_0 = 10[\mathrm{Ba^{2+}}]_0$
integrated rate law (linear plot):	$\dfrac{1}{[\mathrm{Ba^{2+}}]} = kt + \dfrac{1}{[\mathrm{Ba^{2+}}]_0}$	$\ln\dfrac{[\mathrm{SO_4^{2-}}][\mathrm{Ba^{2+}}]_0}{[\mathrm{Ba^{2+}}][\mathrm{SO_4^{2-}}]_0} = k([\mathrm{SO_4^{2-}}]_0 - [\mathrm{Ba^{2+}}]_0)t$	$\ln\left(\dfrac{[\mathrm{Ba^{2+}}]_0}{[\mathrm{Ba^{2+}}]} - \dfrac{1}{10}\right) = k(9[\mathrm{Ba^{2+}}]_0)t$

2. MATERIALS AND METHODS

2.1 Experimental set-up

All experiments were performed with a multimode silica optical fibre FP200ERT (Thorlabs Inc. Newton, New Jersey, USA). The fibre consists of a pure silica core with a low hydroxyl content and an acrylic polymer cladding coated by a Tefzel® layer (figure 2). The core diameter is 200 ± 5 μm, the cladding diameter is 225 ± 5 μm and the coating diameter is 500 ± 30 μm. For the experiments a window of exposed core with a length of 20 mm was created by removing first the coating of the fibre. In a second step the cladding was carefully peeled off with a scalpel under an optical microscope to ensure complete removal of the cladding and an undamaged surface of the fibre core. For each new experiment a new fibre was used and a core exposing window created. Table 2 summarises the refractive indices of the used materials.
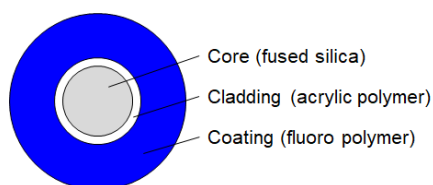
Fig. 2: Cross section of the optical fibre.

Tab. 2: Refractive indices (n) of the relevant materials at 589 nm and ambient temperature. The critical angle θ_{cr} increases (and thus TIR decreases) with an increasing quotient n_2/n_1 of the refractive indices of the environment (n_2) and the core (n_1).

material	n	n_2/n_1	θ_{cr}	reference
fused silica (core)	1.459	--	--	Thorlabs Inc. 2020
cladding polymer	1.365	0.936	69.4°	Thorlabs Inc. 2020
water	1.334	0.914	66.1°	Hale and Querry 1973
4,3 M NaCl brine	1.395	0.956	72.9°	Tan and Huang 2015
barite crystals	1.636	>1	no TIR	Radhakrishnan 1951

The fibre was on one end connected to a light source consisting of a white light emitting halogen lamp (HL-2000-FHSA, Ocean Optics, Largo FL, USA). The other end of the fibre was plugged into a spectrum analyser AQ6370 (Yokogawa Electrical Corp., Tokyo, Japan). A part of the fibre comprising the window of exposed core was inserted into the reaction vessel. For the experiments at room temperature and ambient pressure a polymer beaker on a magnetic stirrer was used. Experiments at elevated temperature were carried out in an autoclave (stainless steel with PTFE insert, BR-300, Berghof GmbH, Eningen, Germany), using two lid openings equipped with HPLC tubing fittings to ensure airtight sealing (Reinsch et al. 2013). The fibre has to be handled carefully as the exposed part is extremely fragile and has to be kept free of bending stress and tensile stress. A scheme of the autoclave set-up is depicted in figure 3.
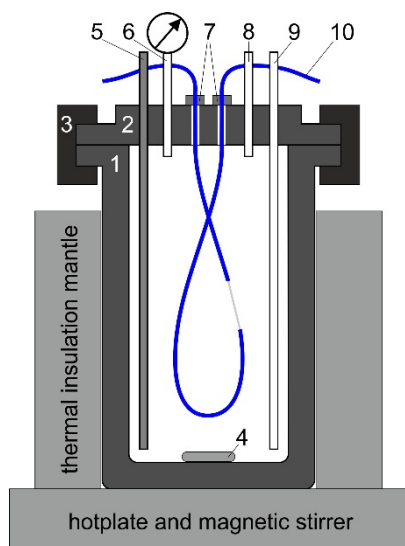
Fig. 3: Experimental set up: Laboratory autoclave with the optical fibre that exhibits a window with exposed fibre core. 1: autoclave cylinder, 2: autoclave lid with inlets, 3: high pressure clamps, 4: stirring rod, 5: thermo couple, 6: capillary with pressure gauge, 7: fibre inlets with airtight fittings, 8: capillary with valve for gas load and pressure release, 9: capillary with valve for liquid injection and sampling, 10: optical fibre.

2.2 Experimental procedure

In order to ensure a complete precipitation within a short reaction time a high oversaturation of barite was intended. The concentrations of the ions in the synthetic fluids were therefore chosen several times higher than typically found in saline geothermal brines from sedimentary reservoirs such as the North German Basin: 1 mmol/l in case of barium

(four times higher) and 10 mmol/l in case of sulfate (approximately seven times higher). For the geothermal plant of Groß Schönebeck, Regenspurg et al. (2010) reported concentrations of 0.25 mol/l for barium ions and 1.5 mol/l sulfate ions in the geothermal fluid. For the barite precipitation experiments, 250 ml of a 1 mmol/l $BaCl_2$ solution were filled into the reaction vessel immersing the exposed fibre window completely. The reaction was initiated by adding 2.5 ml of a 1 mol/l Na_2SO_4 solution resulting in a final concentration of 1 mmol/l Ba^{2+} (137.3 mg/l) and 10 mmol/l SO_4^{2-} (960.6 mg/l). Signals obtained by the spectral analyser were recorded approximately every 1.5 seconds for an experimental duration between 5 and 15 minutes. Experiments were conducted at room temperature and at 150 °C. Experiments at elevated temperatures were prepared by heating the $BaCl_2$ solution in the autoclave until the temperature was constant before adding the Na_2SO_4 solution. Within the autoclave, pressures between 2.7 and 3.1 bar were reached at 150 °C. $BaCl_2$ solutions were prepared with NaCl concentrations of 0, 0.5, 1, 2 and 5 mol/l as background salinity whereas the solution with the latter mimicking the ionic strength of typical geothermal fluids of sedimentary basins (Wolfgramm et al. 2004).

The spectrum analyser measured the light intensity in dependence of the wave length by sweeping through a spectral range from visible to infrared light. The light power over a wavelength window between 1510 and 1590 nm was recorded and analysed. In this range the fibre shows very low absorption of the core material itself. The mean value of the light power averaged over this 80 nm wave length window was calculated. The refractive index depends on the wavelength of the incident light and is usually measured at 589 nm (table 2). It is assumed that scale-formation-induced changes in critical angles determining the occurrence of TIR are similar also at wavelengths between 1510 and 1590 nm. The applicability of near infrared light for fibre-optical sensing of scale-formation was shown by Okazaki et al. (2015).

Each experiment but one was repeated twice. The experiment at room temperature with 1 mol/l NaCl matrix salinity was repeated only once. The attenuation of the light signal was averaged over all repetitions of each experiment and plotted in dependence of time.

After the experiments the fibre was removed and the exposed core part cut out. This part was rinsed with deionised water, air dried and investigated by field emission scanning electron microscopy (FE-SEM; Ultra Plus, Carl Zeiss). High resolution images of the fibre surface with barite crystals were obtained using secondary electron detector at an acceleration voltage from 2 to 5 kV with 30 μm aperture size. Precipitates on the fibres were analysed for its elemental composition using EDX-spectroscopy (Thermo Fisher) at an operating condition of 20 kV acceleration voltage with 30 μm aperture size.

Fluid samples were taken after the experiments, filtered through 45 μm cellulose acetate filters and analysed with inductively coupled plasma - optical emission spectroscopy (5110 ICP-OES, Agilent Technologies). The residual concentration of Ba^{2+} was measured and converted to the amount of precipitated barite (pr_{barite}(meas) in mmol/l) for comparison with the calculated values (table 2).

2.3 Data evaluation

Geochemical modelling with PHREEQC (version 3.8, Pitzer database) was performed to calculate supersaturation and estimate the influence of temperature and ionic strength in the precipitation as well as the maximum amount of barite that can be expected to precipitate (Parkhurst and Appelo 2013).

The measured attenuation is sensitive to the length of the fibre, the length of the exposed core window and the accuracy of the connections of the fibre ends with the light source and the spectral analyser. Therefore, the starting point attenuation was considerably varying from one experiment to another (figure 4 left) due to the fact that the manual preparation of each fibre lead to unique fibres with always slightly different properties affecting the attenuation. In order to make the results comparable the curves had to be normalised and averaged over all repetitions measured (figure 4 right). For each experiment the expected maximum amount of precipitated barite under the given reaction properties in relation to the volume of solution (pr_{barite}(calc) in mmol/l) was calculated using PHREEQC (table 3). The signal data were transformed under the assumption that the maximum recorded change in attenuation

can be related to the maximum amount of barite that is expected to precipitate until equilibrium/saturation as in equation (5). The values were converted to the precipitated amount of barite ($pr_{barite}(t)$ in mmol/l) by applying equation (6). Values of the Ba^{2+}-concentration in solution were calculated according to equation (7).

(5) $$\frac{\Delta A(t)}{\Delta A_{max}} = \frac{pr_{barite}(t)}{pr_{barite}(calc)}$$

(6) $$pr_{barite}(t) = \frac{A(t) - A_0}{A_{max} - A_0} \cdot pr_{barite}(calc)$$

(7) $$[Ba^{2+}](t) = [Ba^{2+}]_0 - pr_{barite}(t)$$

3. RESULTS AND DISCUSSION

The calculated values of the expected barite precipitation show a small dependence from temperature and are always above 97% (table 3). At both temperatures a 99% precipitation of barite from water is expected. At higher ionic strength and the high temperature the calculated barite precipitation decreases slightly with values between 97 and 99%. The same trend is exhibited by the ICP-OES measurements whereas the values (averaged over all experiment repetitions) are even higher with always over 99%.

Tab. 3: Amount of precipitated barite at equilibrium from a starting solution with $[Ba^{2+}]_0$ = 1 mmol/l and $[SO_4^{2-}]_0$ = 10 mmol/l calculated by PHREEQC and measured with ICP-OES.

| background [NaCl] (mol/l)	pr_{barite}(calc) at 25 °C (mmol/l)	pr_{barite}(calc) at 150 °C (mmol/l)	pr_{barite}(meas) at 25 °C (mmol/l)	pr_{barite}(meas) at 150 °C (mmol/l)
0	0.990	0.990	0.9993 ± 0.0002	0.9984 ± 0.0012
0.5	0.989	0.987	0.9988 ± 0.0001	--
1	0.989	0.985	0.9970 ± 0.0002	--
2	0.988	0.980	0.9947 ± 0.0014	0.9957 ± 0.0018
5	0.987	0.973	0.9926 ± 0.0004	0.9911 ± 0.0044

The attenuation of a freshly prepared optical fibre was measured to be between 45 and 55 dBm. Figure 4 (left) shows the typical development of the attenuation during a barite precipitation experiment that was conducted three times under the same conditions. These measurements show the strong influence of differently prepared fibres on the attenuation. In order to make the results comparable it was necessary to normalise and average the data as shown in figure 4 (right).
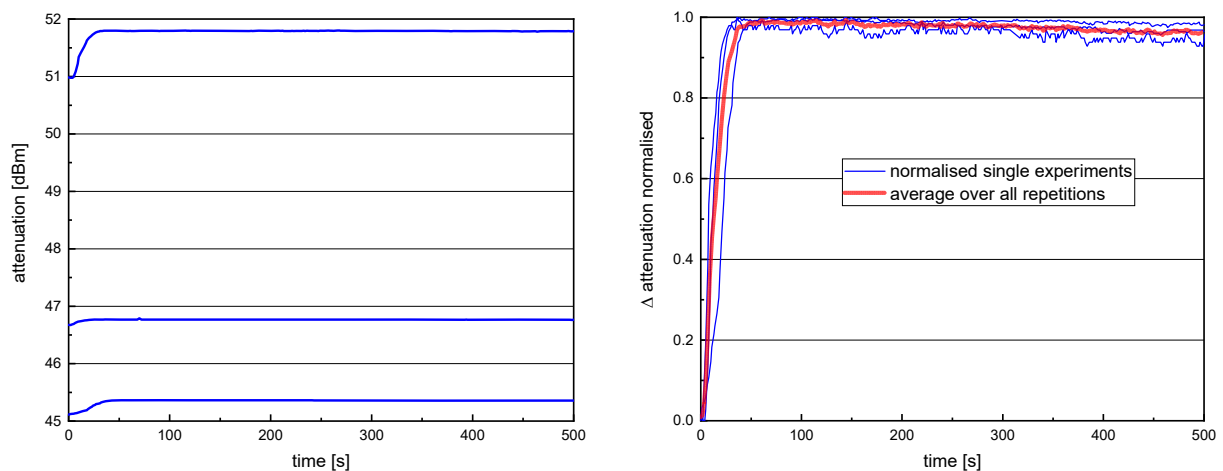
Fig. 4: Left: Attenuation in dependence of the experiment time during $BaSO_4$ precipitation in water at 150 °C for three single experiments, Right: normalised single experiments and averaged curve.

3.1 Effect of temperature and salinity

Barite precipitation kinetics are strongly controlled by salinity and temperature of the solution (e.g. Christy et al. 1993, Risthaus et al. 2001). The results from fibre-optical measurements are summarised in figure 5 showing the remaining Ba^{2+} concentration in solution as calculated from the attenuation values using formula (7) within the first 500 seconds of reaction time. The experiment with the fastest precipitation in water at room temperature was stopped after 5 minutes. Experiments at 150 °C were conducted in solutions of 0, 2 and 5 mol/l NaCl. All curves show a short induction time at the first few seconds with almost no signal change before the precipitation of barite on the fibre increases rapidly. As the barium concentration further decreases the precipitation slows down so that the curves flatten out. The short induction period is attributed to homogeneous nucleation in solution before heterogeneous nucleation on the fibre surface starts. It is also possible that during and shortly after heterogeneous nucleation particles with sizes much smaller than the wavelength of the measured light ($\lambda \approx 1.5$ μm) will appear on the fibre. These particles may be too small to interact with the incident light in a detectable way and thus may be contributing to the induction period. The values of the Ba^{2+} concentration after 500 seconds are still higher than the values expected at the chemical equilibrium that can be derived from table 3. Apparently, the equilibrium is not yet reached after 500 seconds. Differences in the values among the experiments are expected to be influenced by a different extent of the fibre surface coverage with barite crystals. SEM pictures presented in figure 8 indicate different crystal sizes and surface coverages resulting from the different experimental conditions.
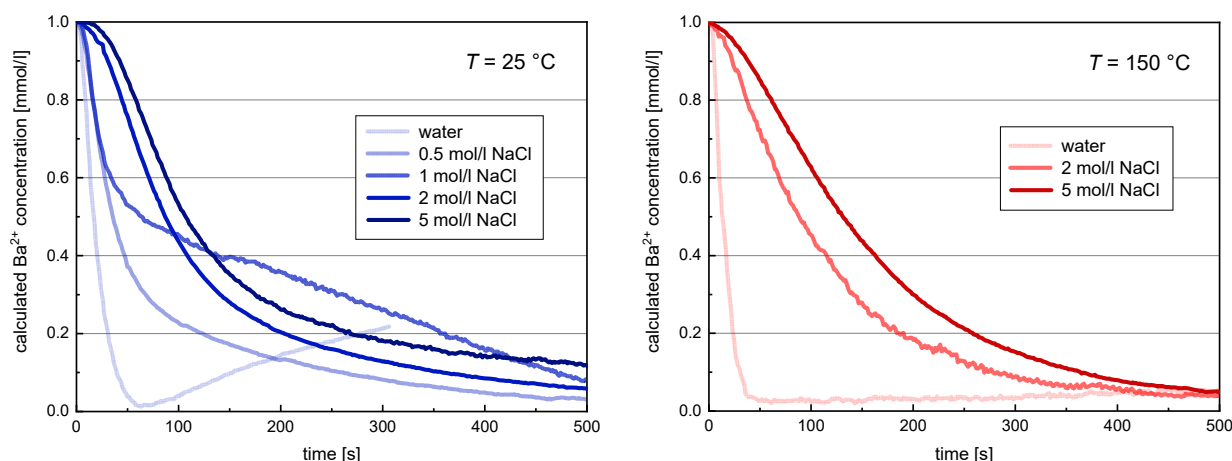
Fig. 5: Calculated Ba^{2+} concentration after barite precipitation in dependence of reaction time at 25 °C (left) and 150 °C (right) with different background salinities. All curves are averages over all repetitions of the respective experiments.

The curve of the experiment in water at 25 °C shows an increase of the barium concentration after the minimum was reached at about 1 minute reaction time. This effect was also observed at the experiment at 150 °C but less pronounced. The underlying signal change cannot be attributed to a real increase of the Ba^{2+} concentration since that would lead to an oversaturated solution again. Instead, it is suspected to be caused by effects on the optical fibre. The fast precipitation of barite crystals on the surface of the fibre from the fluid may lead to a low adhesion and detachment of the crystals in the course of the experiment. Another explanation could be that after the saturation of barite and the equilibrium of dissolution/precipitation was reached very quickly, the growth of a few bigger crystals at the expense of several smaller crystals could lead to a decreasing number of crystals on the fibre and thus to increasing TIR. A similar behaviour was reported by Boerkamp et al. (2017) who investigated a fibre-optical sensor for measurements of heterogeneous crystal growth of calcite scales.

The influence of the temperature on the barite precipitation in the experiments was rather weak. At both temperatures the precipitation rate of the experiments with a given salinity is similar which can be explained by the high oversaturation of the barite in all experiments. This finding is supported by the calculations in table 3 that shows the expected amount of precipitating barite also being similar at different temperatures.
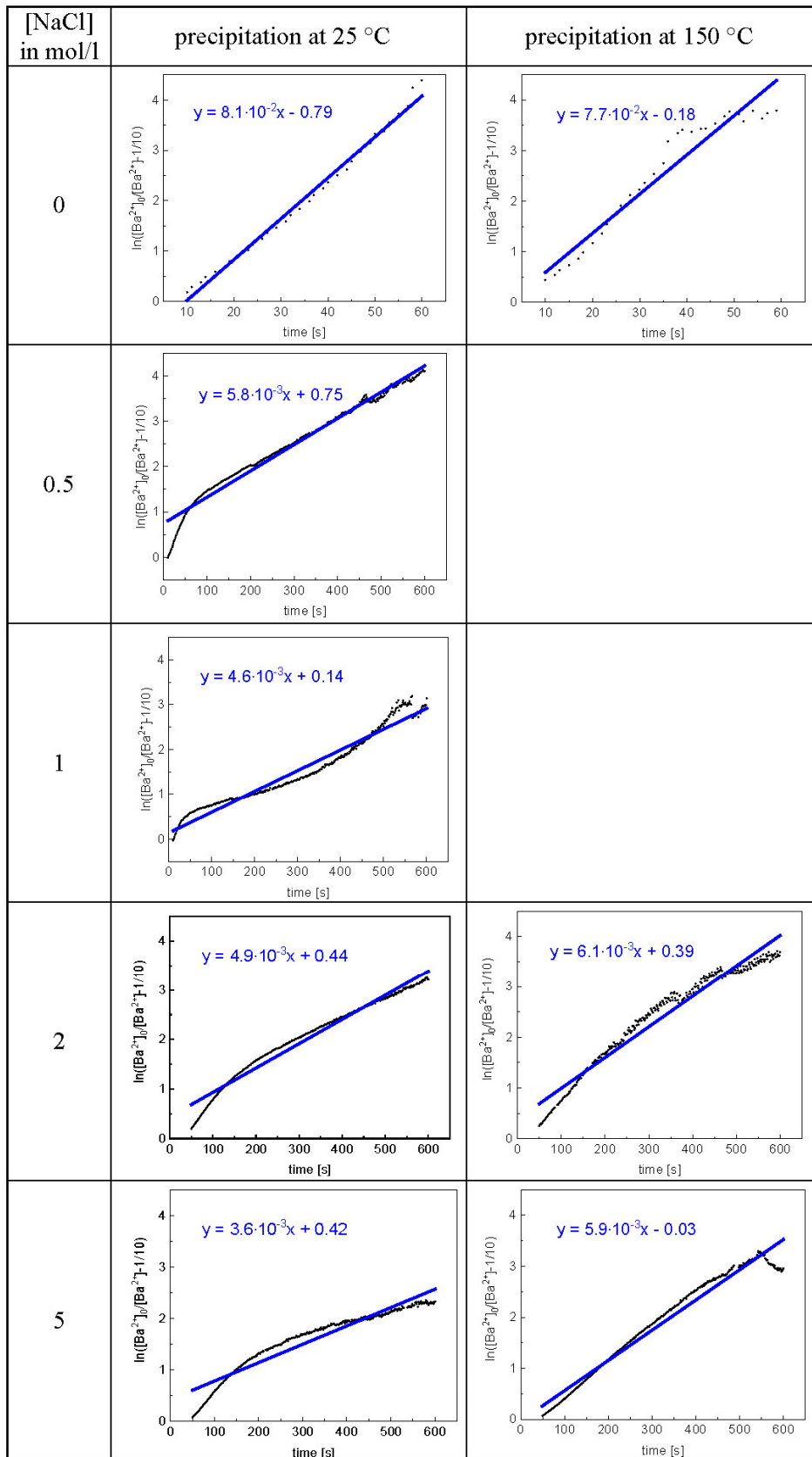
The ionic strength of the solution, however, influenced the barite precipitation rate considerably. The higher the ionic strength the lower was the precipitation rate so that the maximum amount of precipitation at equilibrium is reached later with higher background concentrations of NaCl.

The experiment with 1 mol/l NaCl at room temperature, does not follow the trend as exhibited by the other experiments. It shows an unexpected nearly linear decrease of the precipitation rate after about 50 s of reaction time. The repetition of the experiment showed a similar trend resulting in the averaged curve shown in figure 5 (left). The explanation for that anomaly is assumed to be either a biased error at these measurements such as an unnoticed change of one of the environmental conditions or a different crystal growth process during precipitation leading to a different morphology of the crystals.

3.2 Kinetic derivations

The integrated rate law (table 1) as logarithmic function of the Ba^{2+}-concentration in dependence of time was plotted and showed a nearly linear curve progression. A linear fitting was carried out as shown in figure 6 and rate constants were calculated according to formula (8). A short induction period during the first few seconds of the experiments is attributed to a homogeneous nucleation in solution which was not detectable by the fibre so that the data derived from fibre-optical measurements within this period do not follow the rate law. This time period of 10 seconds for the fast reactions with NaCl concentrations from 0 to 1 mol/l and of around 50 seconds for the other experiments was therefore excluded from the linear fitting. Furthermore, since the rising signal of the experiments with no NaCl does not represent the course of the precipitation reaction at both temperatures, the linear fitting of the integrated rate law was limited to the first minute of these two experiments. In table 4 the considered time interval for the linear fitting for each experiment is given and the values of the determination coefficient (R^2) as well as the obtained values for the rate constants (k) as calculated according to rate law in table 1 are summarised.

(8) $k = slope/(9[Ba^{2+}]_0)$

[NaCl] in mol/l	precipitation at 25 °C	precipitation at 150 °C
0	$y = 8.1 \cdot 10^{-2}x - 0.79$	$y = 7.7 \cdot 10^{-2}x - 0.18$
0.5	$y = 5.8 \cdot 10^{-3}x + 0.75$	
1	$y = 4.6 \cdot 10^{-3}x + 0.14$	
2	$y = 4.9 \cdot 10^{-3}x + 0.44$	$y = 6.1 \cdot 10^{-3}x + 0.39$
5	$y = 3.6 \cdot 10^{-3}x + 0.42$	$y = 5.9 \cdot 10^{-3}x - 0.03$

Fig. 6. The function $\ln([Ba^{2+}]_0/[Ba^{2+}]-1/10) = f(t)$ for all experimental setups. The solid lines represent the linear fits with the function $y = f(x)$ as given in the diagrams.

Tab. 4: Time interval of the linear fitting, determined values of the determination coefficient of the linear fit R^2 and the derived rate constant k for the different experimental conditions.

T (°C)	[NaCl] (mol/l)	time interval (s)	R^2	$k \left(\frac{1}{\text{mol·s}}\right)$
25	0	10 - 60	0.989	9.019 ± 0.168
25	0.5	10 - 600	0.976	0.642 ± 0.005
25	1	10 - 600	0.954	0.513 ± 0.006
25	2	50 - 600	0.968	0.546 ± 0.005
25	5	50 - 600	0.910	0.398 ± 0.007
150	0	10 - 60	0.931	8.607 ± 0.427
150	2	50 - 600	0.957	0.673 ± 0.008
150	5	50 - 600	0.964	0.658 ± 0.007

The determination coefficient R^2 of the linear fitting was always higher than 0.9, thus strongly supporting the assumption that the barite precipitation follows a second order reaction kinetic as derived from the chemical equation (4) and proposed by several other studies (Christy and Putnis 1993, Kühn et al. 1997, Banks et al. 2014). The effect of the temperature is relatively low leading to a slight increase of the rate constant at 150 °C compared to 25 °C but only for the precipitations with a high background salinity of 2 (increased by 0.127 l·mol^{-1}·s^{-1}) and 5 mol/l NaCl (increased by 0.26 l·mol^{-1}·s^{-1}). However, the rate constant shows a strong non-linear decrease with increasing ionic strength that can be explained by the decrease of the mean activity coefficients of the Ba^{2+} and SO_4^{2-} ions in presence of high concentrations of matrix electrolytes so that barite supersaturation is decreasing with increasing salinity (Risthaus et al. 2001). At 25 °C the rate constant drops from 9.0·to 0.4 l·mol^{-1}·s^{-1} whereas at 150 °C the decrease is very similar from 8.6 to 0.6 l·mol^{-1}·s^{-1}. However, the value for the rate constant at 25 °C and with 1 mol/l NaCl (0.513 l·mol^{-1}·s^{-1}) was determined to be slightly lower than the value for the rate constant at 2 mol/l NaCl at the same temperature (0.546 l·mol^{-1}·s^{-1}). This deviation from the trend is attributed to the unexpected decrease of the precipitation rate as shown in figure 5 (left).

Earlier studies using synthetic fluids with high salinity lead to significantly lower rate constants. Banks et al. (2014) determined a rate constant of 0.021 l·mol^{-1}·s^{-1} at 150 °C for barite precipitation from a solution of a salinity similar to a solution with a NaCl concentration between 4 and 5 mol/l. However, they used an only slight excess of the sulfate ion concentration in respect to the barium ion concentration in the starting solution and a different integrated rate law was applied (table 1, column 2) for the rate constant determination.
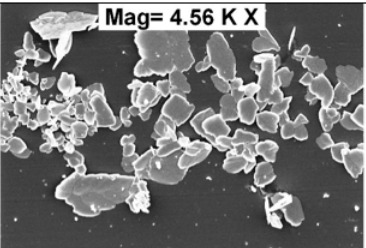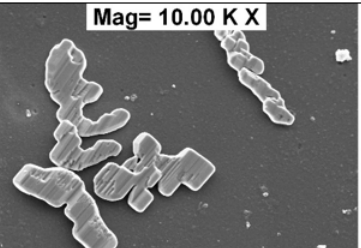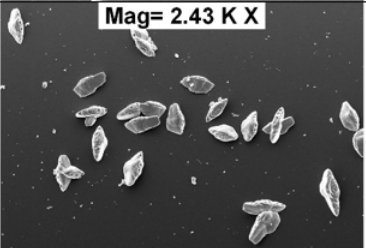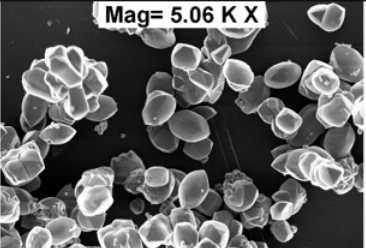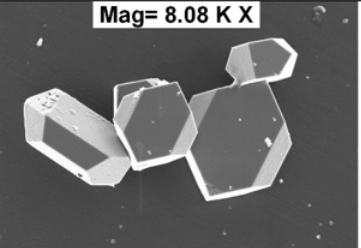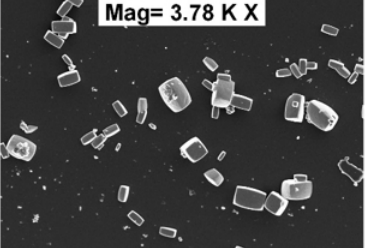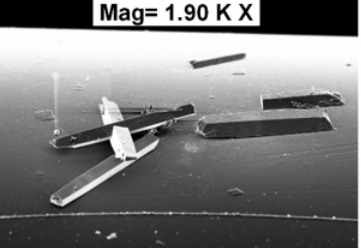
3.2 Characterization of formed barite crystals

Figure 7 and 8 show images from SEM measurements with precipitated barite crystals on the surface of the fibre-optical sensors. EDX measurements determined the precipitates to consist exclusively of barium, sulphur and oxygen confirming the composition of the crystals as being consistent with $BaSO_4$. Figure 7 shows the partial coverage of a fibre core with barite crystals. Shape, size and number of the crystals on the core surface differed for the different reaction conditions (figure 8). At 25 °C the crystal shape changed from small, flat flakes (no NaCl) via oval particles (2 mol/l NaCl) to cuboid crystals (5 mol/l NaCl) with crystal sizes around 1 µm. At 150 °C the shape was rhomboid at 2 mol/l NaCl and changed to elongated rods at the highest ionic strength. At this temperature the crystal size also increased significantly with increasing ionic strength from 1 µm up to 9 µm. The observations can be attributed to the lower precipitation rate at higher temperatures and higher ionic strength conditions that enabled a defined crystal growth. The nucleation rate, that was determined in the kinetic derivations, was also decreasing with increasing temperature and ionic strength so that the number of the resulting scale particles on the fibre core was decreased. A lower amount of crystals with an increased size consequently leads to a lower degree of surface coverage on the fibre

and thus directly influences the evanescent wave resulting in a lower signal attenuation towards the end of the measurements. This effect is assumed to contribute to the slightly higher end-values of the remaining Ba^{2+} concentration after 500 seconds for experiments at elevated salinities and temperature as shown in figure 5.
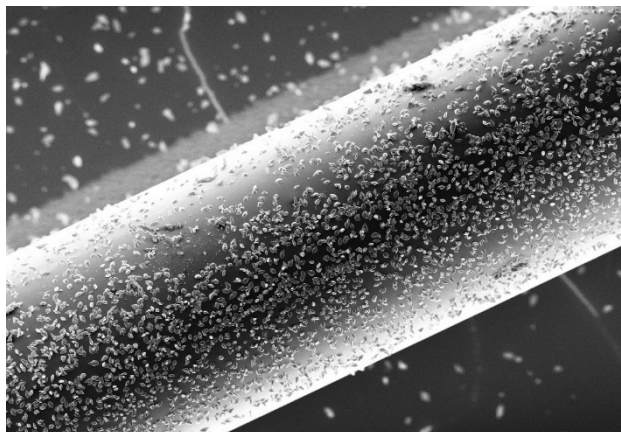
Fig. 7: SEM image of an optical fibre sensor after barite precipitation at 25 °C and 2 mol/l NaCl concentration with 236-fold magnification.

Fig. 8: SEM images of optical fibre sensors after barite precipitation at 25 and 150 °C and background NaCl-concentrations of 0, 0.5, 2 and 5 mol/l. The magnification between 1,900 and 10,000-fold was chosen individually in order to show the general crystal shape. At the concentration of 0.5 mol/l NaCl, only a picture of the crystals that formed at room temperature was available.

With higher temperatures and higher salinities the crystals grow larger in size and with a more defined morphology that indicated a slower rate of crystal growth. The SEM images clearly show an influence of temperature and background salinity on the development of the crystal structures. While crystals formed at 25 °C in water were poorly structured, with increasing temperature and salinity the crystals were more and more developed morphologies. This effect is in agreement with the observations of Banks et al. (2014). Similar results were also reported by Zhang et al. (2019) for calcite precipitates formed in solutions with different NaCl concentrations.

4. CONCLUSIONS

A fibre-optical method for monitoring of the precipitation process and determination of the precipitation rate was developed and tested on the barite system. It was shown that sensing of barite precipitation can be realised with fibre-optical methods at temperatures up to 150 °C and varying salinities. Thus, real-time monitoring of scaling at high temperatures and pressures in an autoclave could be enabled. This way an important shortcoming of existing non-optical detection methods was overcome. It was possible to derive kinetic rate constants using this new method. While the influence of the temperature on the precipitation was rather weak, the salinity was found to have considerable impact on barite precipitation kinetics. High values of the ionic strength were found to decelerate the barite precipitation. In geothermal installations exploiting highly saline fluids with decreased precipitation rates of barite in oversaturated solution, the barite scaling becomes less controllable and demands the application of specific and well-adjusted prevention measures. The strong influence of the fluid salinity on the precipitation rate demonstrates the necessity of applying test methods at the specific temperature and pressure conditions as well as at specific fluid compositions of real geothermal systems for an accurate prediction of scaling risks.

ACKNOWLEDGMENT

DECLARATIONS

Authors' contributions: JZ: consulting and writing of the manuscript, NH: experimental work and data evaluation, SM: SEM measurements and interpretation, TR: consulting, SR: consulting and supervision. All authors read and approved the final manuscript.

Competing interests: The authors declare that they have no competing interests.

REFERENCES

Anderson, G.P., Taitt, C.R., 2008. Evanescent wave fibre optic biosensors. In: Optical Biosensors Second Edition, Elsevier, ISBN 9780444531254, pp. 83-138.

Banks, J., Regenspurg, S., Milsch, H., 2014. Experimental method for determining mixed-phase precipitation kinetics from synthetic geothermal brine. Appl. Geochem. 47, 74-84.

Boerkamp, M., Lamb, D. W., and Lye, P. G., 2007. Using an intrinsic, exposed core, optical fibre sensor to quantify chemical scale formation. In: Journal of Physics: Conference Series, 76, 1. IOP Publishing, p. 012016.

Boerkamp, M., Lamb, D. W., and Lye, P. G., 2013. An intrinsic exposed core optical fibre sensor as a quantitative surface crystallization monitoring sensor. In: Sensors and Actuators B: Chemical 177, 964-969.

Boerkamp, M., Lamb, D. W., and Lye, P. G., 2017. Monitoring the kinetics of heterogeneous crystal growth using an intrinsic exposed core optical fibre sensor. In: Sensors and Actuators B: Chemical 240, 168-173.

Bremer, K., Reinsch, T., Leen, G., Roth, B., Lochmann, S., Lewis, E., 2017. Pressure, temperature and refractive index determination of fluids using a single fibre optic point sensor. Sensors and Actuators A - Physical 256, 84-88.

Canic, T., Baur, S., Bergfeldt, T. and Kuhn, D., 2015. Influences on the Barite Precipitation from Geothermal Brines, Proceedings World Geothermal Congress, Melbourne, Australia, 19-25 April 2015.

Christy, A. G. and Putnis, A., 1993. The kinetics of barite dissolution and precipitation in water and sodium chloride brines at 44-85°C. Geochim. Cosmochim. Acta 57, 2161–2168.

Chyad, R. M., Mat Jafri, M. Z. and Ibrahim, K., 2013. Nano-Optical Fiber Evanescent Field Sensors. In: Advanced Materials Engineering and Technology, 626, Advanced Materials Research. Trans Tech Publications, 1027-1032.

Fidanboylu, K. and Efendioglu, H., 2009. Fibre optic sensors and their applications. In: 5th International Advanced Technologies Symposium 2009, 6, 2-3.

Hale, G.M. and Querry, M.R., 1973. Optical constants of water in the 200-nm to 200-μm wavelength region, Appl. Opt. 12, 555-563.

Harmon, J.P., 2001. Chapter 1: Polymers for Optical Fibers and Waveguides: An Overview. In: Harmon and Noren (Eds.) "Optical Polymers", ACS Symposium Series, American Chemical Society, Washington, DC, pp. 1-23.

Kühn, M., Frosch, G., Kölling, M., Kellner, T., Althaus, E., and Schulz, H. D., 1997. Experimentelle Untersuchungen zur Barytübersättigung einer Thermalsole. Grundwasser - Zeitschrift der Fachsektion. Hydrogeologie 3 (97), 111-117.

MacAdam, J. and Jarvis, P., 2015. Chapter 1 - Water-Formed Scales and Deposits: Types, Characteristics, and Relevant Industries. In: Amjad, Z. and Demadis, K.D. (Eds.) Mineral Scales and Deposits, Elsevier, Amsterdam, 3-23.

Okazaki, T., Imai, K., Tan, S. Y., Yong, Y. T., Rahmn, F. A., Hata, N., Taguchi, S., Ueda, A., and Kuramitz, H., 2015. Fundamental Study on the Development of Fiber Optic Sensor for Real-time Sensing of $CaCO_3$ Scale Formation in Geothermal Water. In: Analytical Sciences 31.3, 177–183.

Okazaki, T., Orii, T., Ueda, A., Ozawa, A., and Kuramitz, H., 2017. Fiber Optic Sensor for Real-Time Sensing of Silica Scale Formation in Geothermal Water. Sci. Rep. 7, 3387.

Parkhurst, D.L. and Appelo, C., 2013. Description of input and examples for PHREEQC version 3: a computer program for speciation, batch-reaction, one-dimensional transport, and inverse geochemical calculations. In: Section A: Groundwater in Book 6 Modeling Techniques, U.S. Geological Survey, Reston, Virginia.

Philip-Chandy, R., Scully, P., and Thomas, D., 2000. A novel technique for on-line measurement of scaling using a multimode optical fibre sensor for industrial applications. In: Sensors and Actuators B: Chemical 71.1, 19-23.

Radhakrishnan, T., 1951. Further Studies on the Temperature Variation of the Refractive Index of Crystals, Proc. Indian Acad. Sci., A33, 22-34.

Regenspurg, S., Wiersberg, T., Brandt, W., Huenges, E., Saadat, A., Schmidt, K. and Zimmermann, G., 2010. Geochemical properties of saline geothermal fluids from the in-situ geothermal laboratory Groß Schönebeck (Germany). Chem. Erde 70 (S3), 3-12.

Regenspurg, S., Feldbusch, E., Byrne, J., Deon, F., Driba, D.L., Henninges, J., Kappler, A., Naumann, R., Reinsch, T. and Schubert, C., 2015. Mineral precipitation during production of geothermal fluid from a Permian Rotliegend reservoir. Geothermics 54, 122-135.

Reinsch, T., Cunow, C., Schrötter, J., Giese, R., 2013. Simple feed-through for coupling optical fibres into high pressure and temperature systems. Measurement Science and Technology, 24, 037001-037003, https://doi.org/10.1088/0957-0233/24/3/037001.

Risthaus, P., Bosbach, D., Becker, U. and Putnis, A., 2001, Barite scale formation and dissolution at high ionic strength studied with atomic force microscopy. Colloids and Surfaces A: Physicochemical and Engineering Aspects 191, 201-214.

Scheiber, J., Seibt, A., Birner, J., Cuenot, N., Genter, A. and Moeckes, W., 2014. Barite Scale Control at the Soultz-sous-Forêts (France) EGS Site, Proceedings of the 38th Workshop on Geothermal Reservoir Engineering Stanford University, Stanford, California, February 24-26, 2014.

Shukla, S.K., Kushwaha, C.S., Gunert, T. and Demir, M.M., 2019. Chemically modified optical fibers in advanced technology: an overview. Optics Laser Tech. 115, 404-432.

Tan, C.Y., Huang, Y.X., 2015. Dependence of Refractive Index on Concentration and Temperature in Electrolyte Solution, Polar Solution, Nonpolar Solution, and Protein Solution. J. Chem. Eng. Data 60, 2827-2833.

Thorlabs Inc. 2020, Optical Fibre Specifications Page visited on May 29th 2020: https://www.thorlabs.com/newgrouppage9.cfm?objectgroup_id=362

Udd, E. and Spillman Jr., W.B. (Editors), 2011. Fiber Optic Sensors: An Introduction for Engineers and Scientists, 2nd Edition, John Wiley and Sons, Hoboken, New Jersey, ISBN: 978-0-470-12684-4.

Vardeny, Z.V. 2002. Telecommunications: A boost for fibre optics, Nature 416, 489-491.

Wallace, A., Boerkamp, M., G. Lye, P.G., Lamb, D.W., Doherty, W.O.S., Fellows, C.M., 2008. Assessment of an Intrinsic Optical Fiber Sensor for in Situ Monitoring of Scale-Forming Salts. Industrial & Engineering Chemistry Research 47, 1066-1070.

Wang, X. and Wolfbeis, O.S., 2016. Fibre-optic chemical sensors and biosensors. Anal. Chem. 85, 203-227.

Wolfgramm, M., Seibt, A., and Kellner, T., 2004. Stimulation tests in a deep Rotliegend sandstone formation - geochemical aspects. In: Sandsteine im In-situ-Geothermielabor Groß Schönebeck, STR04/03 Geothermie Report 04-01, 143.

Yuan, M. D. and Todd, A. C., 1991. Prediction of sulfate scaling tendency in oilfield operations. Society of Petroleum Engineers, SPE 18484, 63-72.

Zhang, D., Lin, Q., Xue, N., Zhu, P., Wang, Z., Wang, W., Ji, Q., Dong, L., Yan, K., Wu, J., and Pan, X., 2019. The kinetics, thermodynamics and mineral crystallography of $CaCO_3$ precipitation by dissolved organic matter and salinity. In: Science of the Total Environment 673, 546–552.

Zotzmann, J., Vetter, A. and Regenspurg, S., 2018. Evaluating Efficiency and Stability of Calcite Scaling Inhibitors at High Pressures and High Temperatures in Laboratory Scale. Geothermal Energy 6, 18.